Supporting information

Switching CO_2 Electroreduction on Copper between C_2 Products and HCOOH by Ionic Surfactants

Sulan Peng,[#a] Minxing Shu,[#a] Shiyi Ge, [a] Ye Liu, [a] Jingnan Xv, [a] Rongrong Li, [a] Jiayi Wei, [a] Kailin Chen, [a] Qiming Yu,[*a] Hongming Wang[*ab]

[a]College of Chemistry and Chemical Engineering, Nanchang University, Nanchang 330031, China

[b]Jiangxi Provincial Key Laboratory of Functional Crystalline Materials Chemistry, Nanchang University, Nanchang 330031, China

1. Experimental Methods

Chemicals and materials: All experimental chemicals were purchased from suppliers and used directly without further purification. Copper nitrate ($Cu(NO_3)_2$ and cetyltrimethylammonium bromide (CTAB, 99 %) were purchased from Anhui Zesheng Technology Co., Ltd. Sodium hexadecyl sulfate (SDS_{16}, 99 %), sodium tetradecyl sulfate (SDS_{14}, 95 %), and sodium dodecyl sulfate (SDS_{12}, 95 %) were purchased from Beijing Innochem Technology Co., Ltd. Potassium hydroxide (KOH, 99.7 %) and ethanol (C_2H_5OH, 98 %) were purchased from China National Pharmaceutical Group Co., Ltd. Carbon dioxide (CO_2) and argon (Ar) were supplied by Nanchang Jiangzhu Bamboo Industry Co., Ltd. All aqueous solutions were prepared using Milli-Q (DI) water (>18 MΩ) purified through a Sartorius Arium mini ultrapure water system.

***Synthesis of CuO*:** In a typical process[1], CuO nanopowder was prepared via precipitation from a copper nitrate solution using an excess of KOH (40 wt %). The obtained black precipitate was thoroughly washed with distilled water until the effluent reached a neutral pH, followed by filtration and drying in air at ambient temperature over two days.

Working Electrode Preparation: A catalyst ink was prepared by dispersing 0.5 mg of catalyst powder in a mixture of 1 mL isopropanol and 100 μL Nafion binder, followed by ultrasonication for 15 minutes to form a homogeneous suspension. The ink was then uniformly coated onto the active area (2×0.5 cm^2) of a carbon paper substrate (SGL Sigracet 22BB, total size: 3×1.5 cm^2).

Electrolyte Preparation: We prepared the modified electrolytes by dissolving specific ionic surfactants in a 1 M KOH solution. The additives comprised a series of anionic sodium alkyl sulfates (SDS_{12}, SDS_{14}, SDS_{16}) and the cationic surfactant CTAB, with concentrations maintained in the sub-millimolar range (0.02 - 0.1 mM) to form homogeneous solutions for interfacial engineering.

2. Characterization

A suite of characterization techniques, including SEM, TEM, XRD, and XPS, was employed to analyze the samples. Scanning electron microscopy (SEM) was conducted on Quanta 200FEG. Transmission electron microscopy(TEM) was conducted on JEM-2100, high-resolution TEM (HRTEM) and corresponding energy-dispersive spectroscopy (EDS) were performed on a Themis Z and the lattice spacing of each sample was measured from corresponding area in HRTEM images.

X-ray diffraction (XRD) analysis was performed on the X-ray diffraction (Bruker D8 advance) with Cu-Kα radiation and the scattering range of 2θ was from 10° to 80°, with a scanning rate of 5° min^{-1}. X-ray photoelectron spectroscopy (XPS) characterization was conducted on Thermo Scientific K-Alpha using 200 W monochromatic Al Kα (1486.6 eV) radiation under a pressure of 3×10^{-10} mbar, all the XPS spectra were calibrated by the C 1s peak at 284.4 eV.

3. Electrochemical measurements

The electrochemical CO_2 reduction measurements were conducted in a flow cell controlled with an electrochemical workstation (CHI760E). The flow cell consists of three independent chambers: catholyte (gas diffusion electrode, SGL Sigracet 28 BC), gas, and anolyte (Platinum flakes, 1 mm in thickness). The Ag/AgCl reference electrode is placed into the catholyte chamber through a drilled top hole. An anion exchange membrane (Fumasep FAB-PK-130) is employed to separate the anolyte and catholyte chambers. The working electrode was prepared by spray-coating a pre-made catalyst ink *via* an airbrush on the gas diffusion electrode with a size of 2*0.5 cm^2. The catalyst loading is 1mg cm^{-2} to ensure similar particle density. 1 M aqueous KOH solution was circulated into both the anode and cathode chambers at a constant flow rate of 10 ml min^{-1} with the assistance of a dual-channel peristaltic pump. A high-purity CO_2 gas flow of 20 cm^3 min^{-1} was supplied to the gas chamber for CO_2RR tests; for the carbon source verification experiment, high-purity Ar gas at the same flow rate was used (all other conditions unchanged). The gas flow was precisely controlled by a digital mass flow controller (Sevenstar D07-19B)

Gaseous CO_2 reduction products were analyzed online using a gas chromatograph (GC, Fuli GC9790 Plus) equipped with both a flame ionization detector (FID, for CO, CH_4, C_2H_4, and C_2H_6) and a thermal conductivity detector (TCD, for H_2). Liquid products were collected from the cathode compartment. For ethanol, we only analyze the content of ethanol in the products by headspace-gas chromatography (HS-GC), while formic acid was determined by ^{1}H NMR spectroscopy.

All the potentials were converted to RHE, according to the equation

$$E\ (vs.\ RHE) = E\ (vs.\ Ag/AgCl) + 0.059\ pH + 0.198.$$

Electrode intrinsic properties of the analyzed materials were evaluated on a three-electrode system using an Ag/AgCl electrode as the reference electrode, graphite as the counter electrode.

The flow rate of CO_2 was maintained at 20 mL min^{-1} by a mass flowmeter during electrochemical measurements. The LSV measurements were conducted at a scan rate of 5 mV s^{-1} in a KOH solution (1 M). The ECSAs of the prepared catalysts were compared by measuring their double layer capacitances calculated from the corresponding cyclic voltammetry curves in the potential window from -0.24 to -0.14 V vs. RHE. The EIS experiments for CO_2 reduction at the open-circuit potential were performed at a small (5 mV) AC voltage in a frequency range from 10 MHz to 100 kHz.

The FE of the gas products was calculated as follows:

$$\mathrm{FE} = \frac{Q_{product}}{Q_{total}} \times 100\% = \frac{(\frac{v}{60\ \mathrm{s\ min^{-1}}}) \times (\frac{y}{24000\ \mathrm{cm^3\ mol^{-1}}}) \times \mathrm{N} \times \mathrm{F}}{j} \times 100\%$$

Where v is the CO_2 flow rate (20 mL min^{-1}); y is the concentration of gas in an 1 mL quantitative loop (ppm); N is the electron transfer number; F is the Faraday constant (96485 C mol^{-1}); and j is the total current density (A cm^{-2}).

The FE of the liquid products: $Q_{product}$ and Q_{total} were obtained using the following equations:

$$Q_{product} = Z_{product} \times F \times N_{product}$$

$$Q_{total} = I \times t$$

Therefore, FE_{liquid} can be written as

$$FE_{liquid} = \frac{Z_{product} \times F \times N_{product}}{I \times t}$$

$Z_{product}$ is the number of electrons exchanged for the product formation; $N_{product}$ is obtained by quantifying the DMSO solution in the H-NMR spectrum as an internal reference calibration.

Electrochemical active surface area (ECSA) calculation: The ECSAs of catalysts were calculated based on their electrical double layer capacitor (C_{dl}), which were obtained from CV plots in a narrow non-Faradaic potential window from -0.24 to -0.14 V (vs. RHE). The measured capacitive current densities at -0.19 V were plotted as a function of scan rate and the slope of the linear fit was calculated as C_{dl}. The specific capacitance was found to be 60 μF cm^{-2}, and the ECSA of the catalyst is calculated from the following equation:

$$\mathrm{ECSA} = C_{dl} / (60\ \mu\mathrm{F\ cm^{-2}})\ \mathrm{cm^2}$$

The intrinsic activity was revealed by normalizing the current to the ECSA to exclude the effect of surface area on catalytic performance.

4. In-situ Raman characterization

Electrochemical in situ Raman spectrometer is a confocal laser Raman spectrometer of Zollihan light /RTS2-301-SMS, the laser is VCL-488nm M0-30W, the light source is 532 nm, the power is 2 mW, and the recorded signal is scanned 4 times and accumulated under the integral of 20 seconds. In-situ Raman spectroelectrochemical cell (3H gas diffusion type) purchased from Wuhan Cosheruian Technology Co., LTD., 1 mg catalyst and 10 μL Nafion solution were added to 1 mL isopropyl alcohol for ultrasonic dispersion, which was evenly sprayed on 1 cm^{-2} GDE with a spray gun and dried with flowing nitrogen, and then nano-gold was sprayed on the surface. The experiment was carried out at 1 M KOH with graphite rod electrode compared with silver chloride electrode. The CO_2 flow rate was 20 mL min^{-1}, and the electrolyte was circulated by peristaltic pump with a flow rate of 20 mL min^{-1}.

5. Surface-enhanced infrared absorption spectroscopy

Surface-enhanced infrared absorption spectroscopy (SEIRAS) in attenuated total reflection (ATR) mode was utilized. A Thermo Nicolet 8700 spectrometer, equipped with a liquid nitrogen-cooled MCT detector, was employed for the electrochemical ATR-SEIRAS measurements. An approximately 60-nm-thick Au thin film was chemically deposited on the Si prism using a "two-step wet process". Prior to the Au deposition, the Si prism surface, which was used for IR reflection, was polished using Diamond suspension and then cleaned by sonicating in water. Subsequently, the prism was immersed in a piranha solution (a 7:3 volumetric ratio of 98% H_2SO_4 and 30% H_2O_2) for 2 hours. 30 μL of ink was deposited onto the Au-film working electrode and allowed to dry. The ink-coated prism was then assembled into a homemade spectroelectrochemical cell, serving as the working electrode. A Hg/HgO reference electrode was introduced near the working electrode through a Luggin capillary. A Pt mesh (1 cm × 1 cm) was used as the counter electrode.

6. Molecular dynamics simulations

Molecular dynamics simulations were carried out using the LAMMPS program. Simulation input files were generated using the charmm2lammps.pl tool available in the LAMMPS distribution and the psfgen plugin of VMD. The initial structures were energy minimized to remove potentially problematic close contacts between atoms. The barostat by Berendsen et al. was used to maintain

the system pressure at 1 atm, with a damping time of 1 ps. The pressure was controlled semi isotropically; Periodic boundary conditions were applied in all 3 dimensions. The SHAKE algorithm was applied, with a relative tolerance of 10^{-5}, to constrain all the bonds involving hydrogen atoms, as well as the H-O-H angle in water. The integration time step was 1 fs. At every step, the net momentum of the mass center of the entire system was removed to prevent any drifting. Nonbonded Lennard-Jones interactions were cut off beyond 10 Å. Electrostatic interactions were computed using the PPPM (particle-particle particle-mesh) method, with a relative error tolerance of 10^{-5}, and a real space cutoff of 10 Å. SPC water model was used.

7. DFT calculations

The plane-wave Vienna Ab-initio Simulation Package (VASP) was applied in all first-principles calculations using projector augmented-wave pseudopotentials with the GGA-type PBE functiona. A model with periodic boundary conditions was used, and the plane wave energy cutoff was set to 450 eV. The reciprocal space for all calculation systems was a Gamma k-point grid with dimensions of 3×3×5. To prevent interactions between replicas along the z-direction, vacuum spacing of at least 20 Å was used between the adjacent images.

The adsorption energy was calculated by the following formula:

$$E_a = E_{final} - E_{substrate} - E_{adsorbate}$$

where E_a, E_{final}, $E_{substrate}$, and $E_{adsorbate}$ are the adsorption energy of the adsorbate on the substrate, total energy of the adsorbate on the substrate, total energy of the substrate, and total energy of the adsorbate, respectively.

The free energy of this reaction was computed via the following equation:

$$\Delta G = E_a + \Delta Z_{PE} - T\Delta S$$

where ΔG, ΔZ_{PE}, and ΔS represent the Gibbs free energy, zero-point energy, and entropy, respectively.

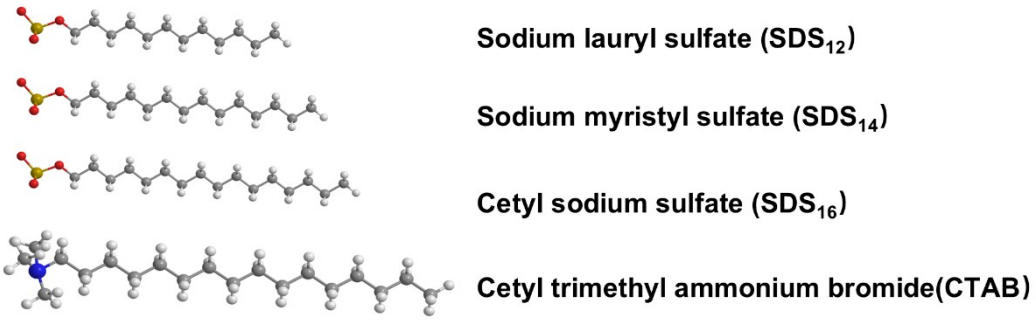

Fig. S1 Tructural formulas of different surfactants.

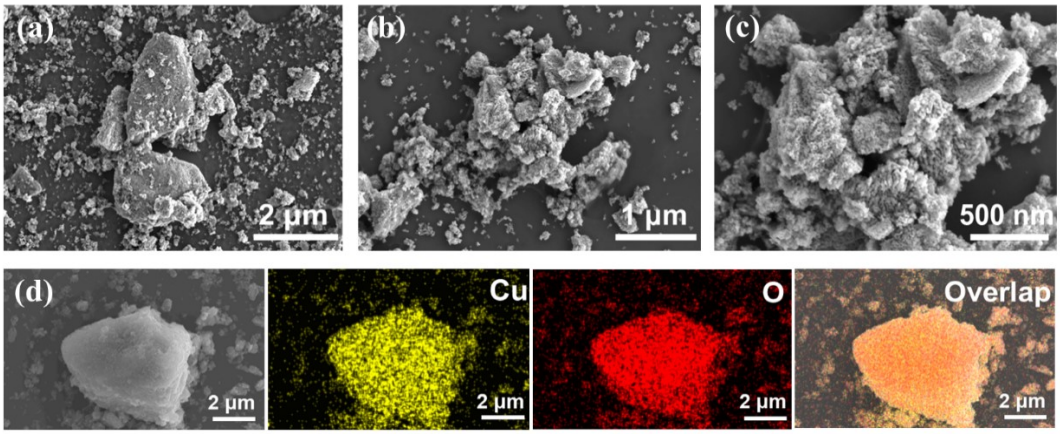

Fig. S2 SEM characterization image of CuO catalyst. SEM spectra of CuO catalyst at (a) 2 μm, (b) 1 μm, and (c) 500 nm, as well as mapping spectra of (d) element distribution.

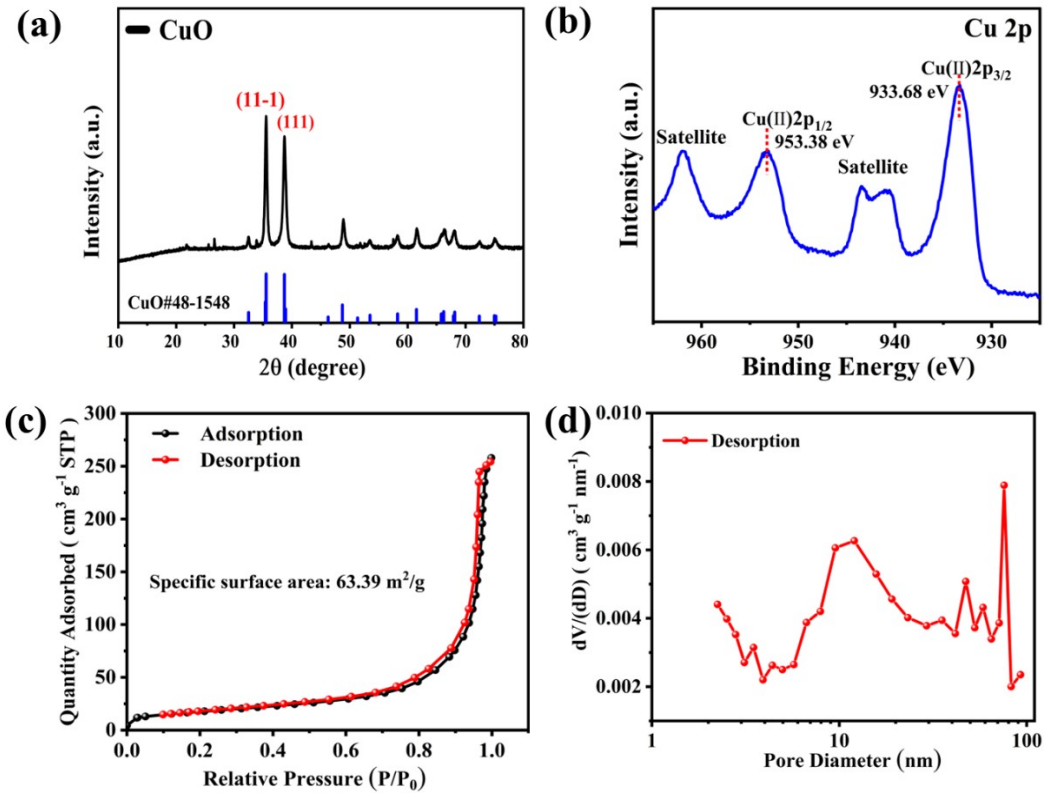

Fig. S3 (a) XRD pattern of the CuO catalyst, (b) The Cu 2p XPS spectrum of the CuO catalyst, (c) N_2 adsorption-desorption isotherms of CuO. (d) The pore size distribution curves of the CuO calculated using BJH model.

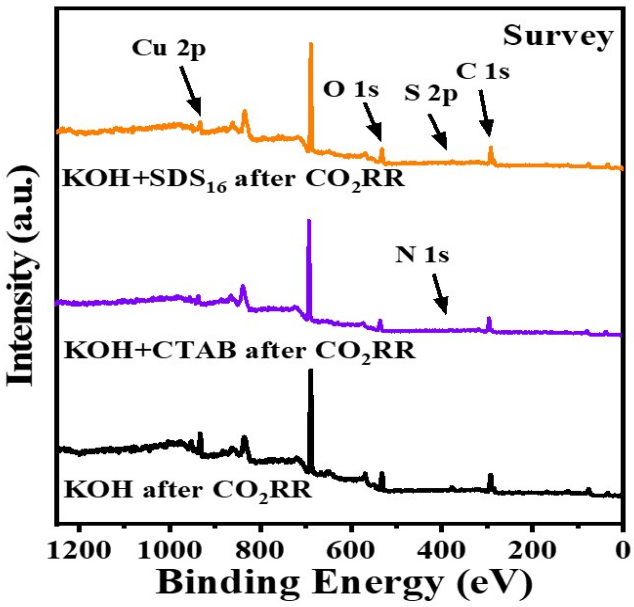

Fig. S4 (a)The total XPS spectrum of 1 M KOH electrolyte modified by anion and cationic surfactants after 1 hour of CO_2RR electrocatalytic reaction.

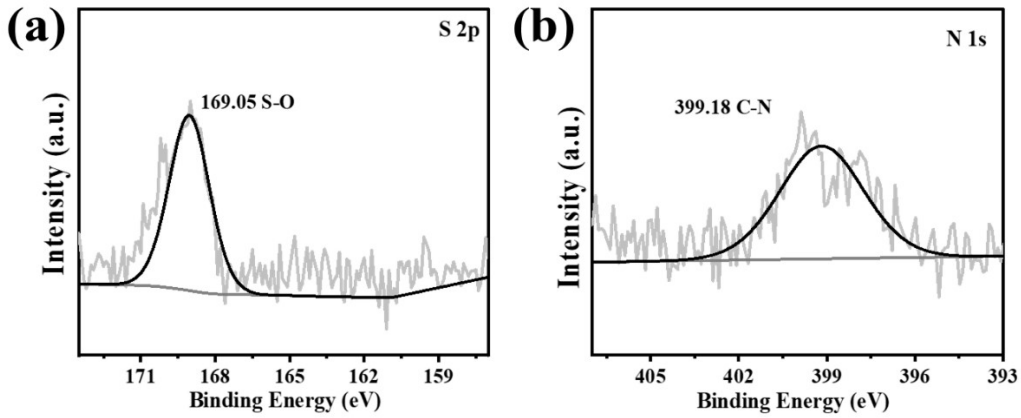

Fig. S5 XPS spectra of S 2p and N 1s of 1 M KOH electrolyte modified by anionic and cationic surfactants after CO_2RR electrocatalytic reaction for 1 h[2,3].

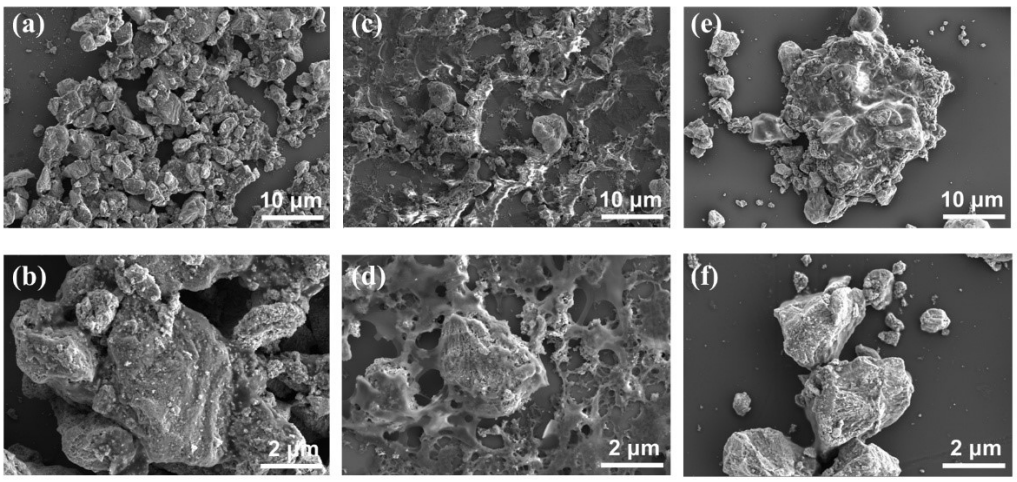

Fig. S6 SEM images of Cu catalysts at 10 µm and 2 µm, corresponding to (a-b) Cu_x(KOH), (c-d) Cu_x(KOH+ SDS_{16}), and (e-f) Cu_x(KOH+CTAB), respectively.

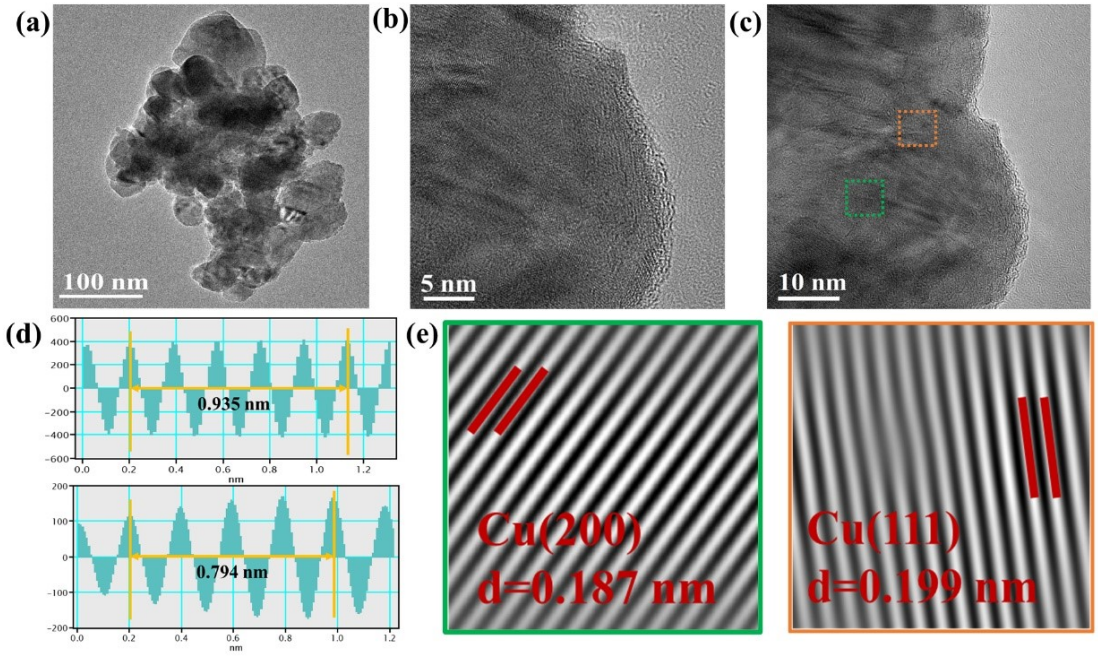

Fig. S7 Under the Cu_x(KOH+ SDS_{16}) electrolyte condition. (a) TEM characterization of Cu; (b-c) HR-TEM image of Cu; (d-e) The lattice spacings corresponding to the (200) and (111) crystal planes of Cu.

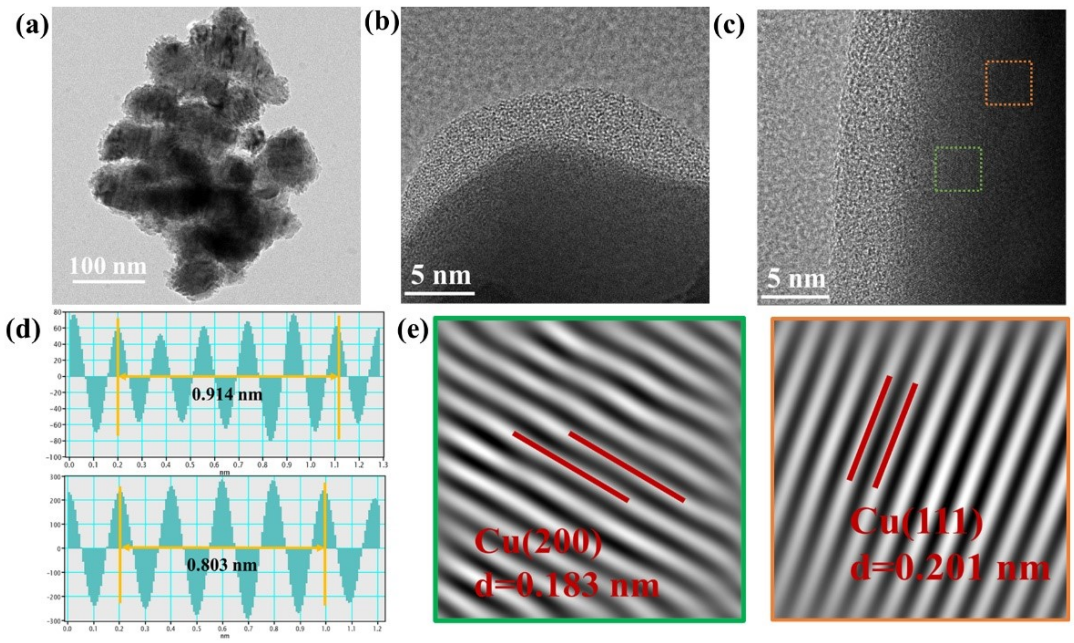

Fig. S8 Under the Cu_x(KOH+CTAB) electrolyte condition. (a) TEM characterization of Cu; (b-c) HR-TEM image of Cu; (d-e) The lattice spacings corresponding to the (200) and (111) crystal planes of Cu.

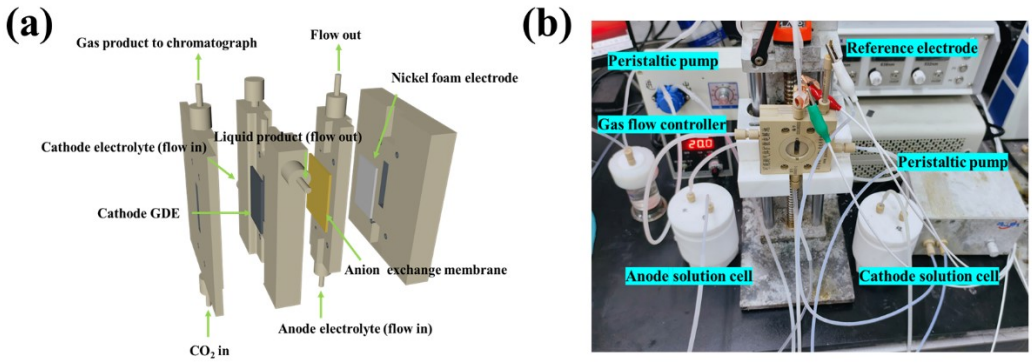

Fig. S9 (a) Schematic diagram of a customized flow cell; (b) Setup of the flow cell for CO_2RR.

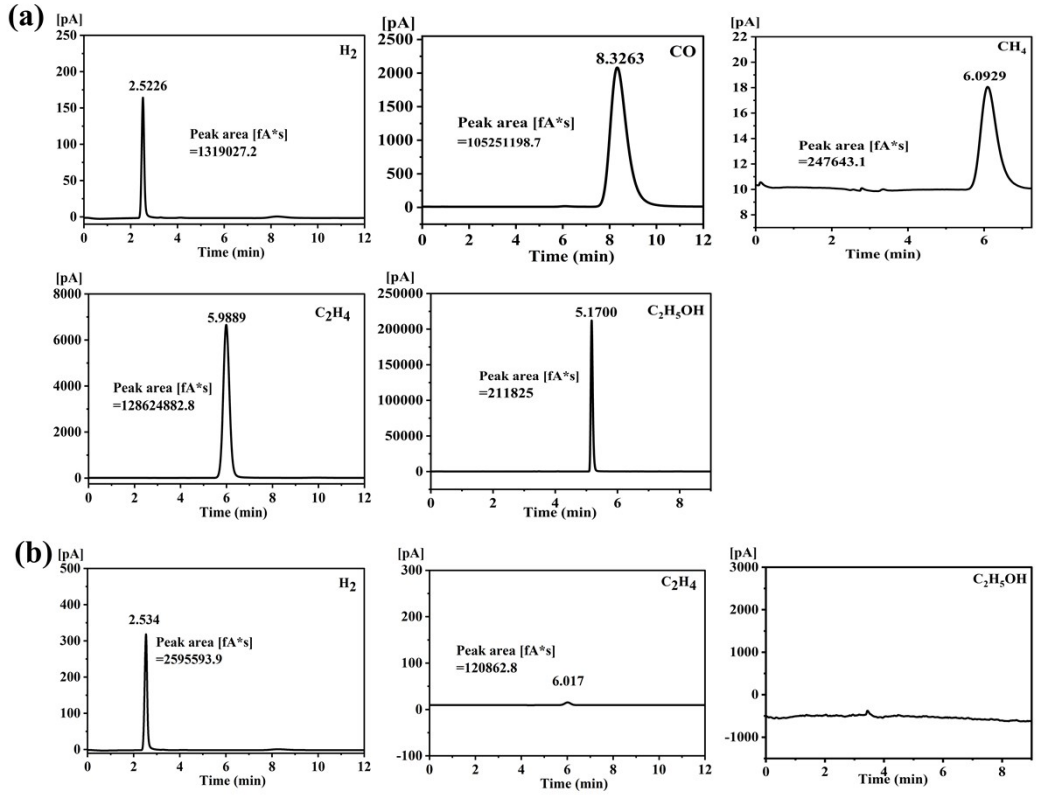

Fig. S10 (a) When the CO_2 reduction reaction is carried out in the Cu_x(KOH+SDS_{16}) system under the condition where (a) CO_2 and (b) Ar saturation, the gas chromatography run curve of the C_2 product is shown when the reference electrode potential is -1.0 V vs. RHE.

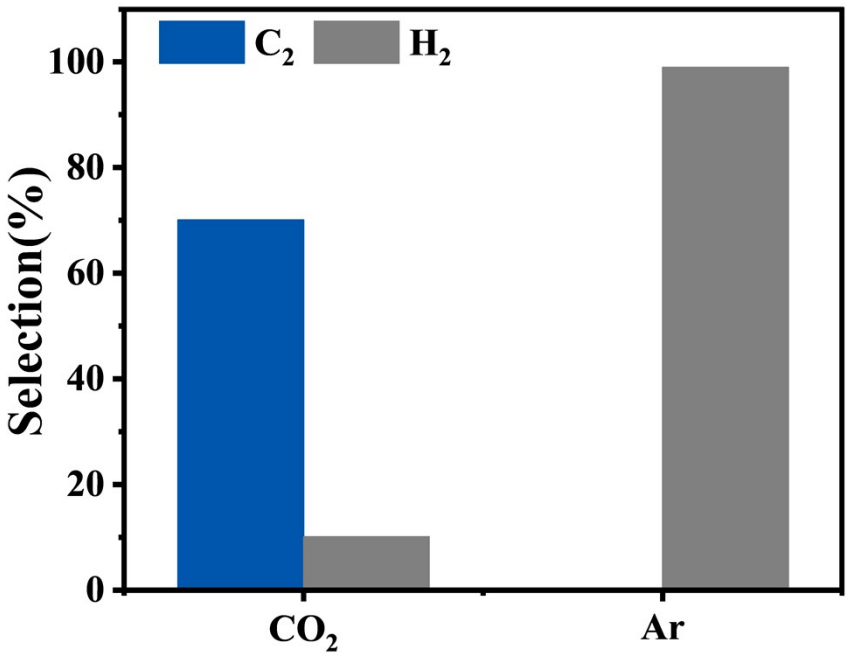

Fig. S11 Faradaic efficiency of C_2 products (C_2H_4+C_2H_5OH) in Cux(KOH+SDS_{16}) system under CO_2/Ar-saturated 1 M KOH electrolyte at -1.0 V vs. RHE.

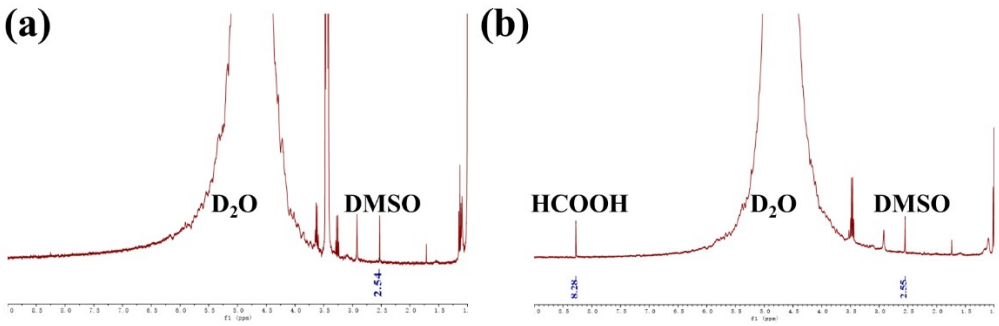

Fig. S12 ^{1}H-NMR spectra of liquid products. (a) Control sample without surfactant; (b) ^{1}H-NMR spectrum of CO_2RR on Cu_x(KOH+CTAB) catalyst at -1.0 V vs. RHE.

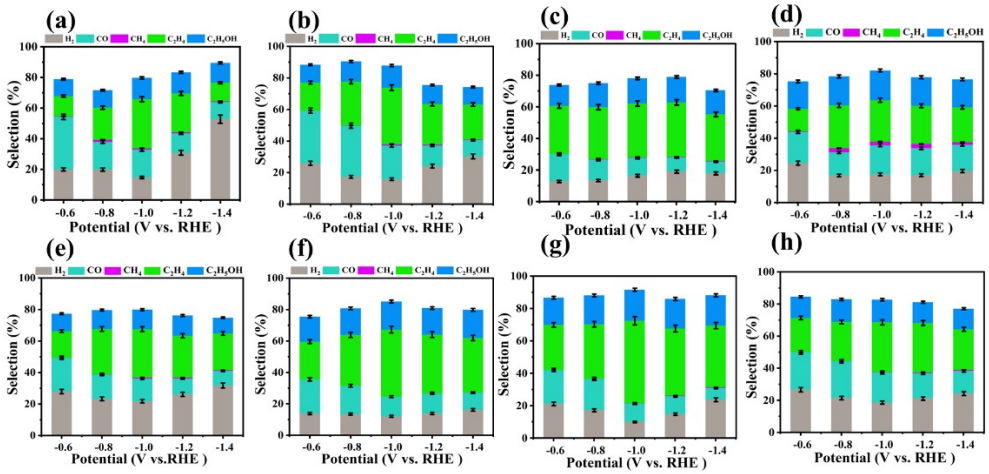

Fig. S13 (a-e) Faradaic efficiency of CO_2RR at various potentials for SDS_{12} concentrations of 0.02, 0.025, 0.05, 0.075, and 0.1 mM, respectively; (f-g) show the dependence of CO_2RR Faradaic efficiency on applied potential in 1 M KOH electrolyte for sodium sulfates with different alkyl chain lengths (SDS_{14}, SDS_{16}) at their respective optimal concentrations identified in this study, measured at -1.0 V vs. RHE; and (h) Faradaic efficiency of CO_2RR in pure KOH electrolyte at -1.0 V vs. RHE.

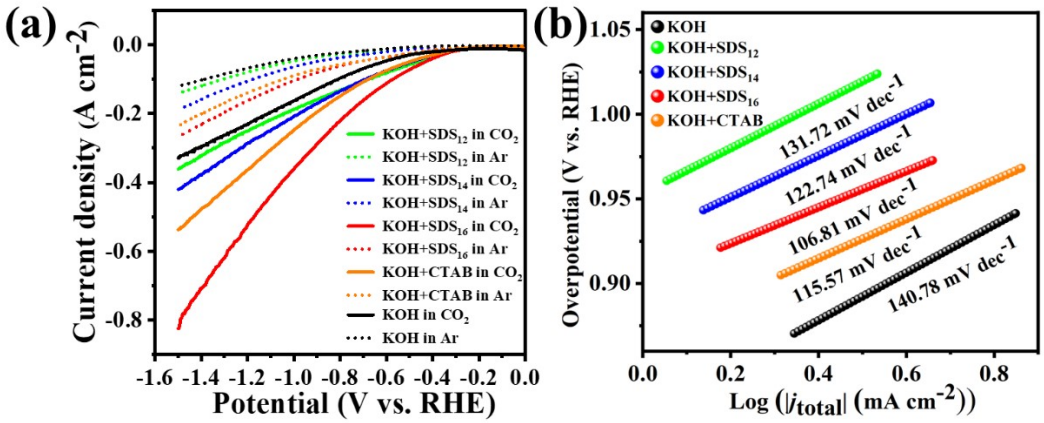

Fig. S14 LSV plots of CuO catalyst at CO_2/Ar saturation in 1 M KOH electrolyte systems without and with SAAs of different alkyl chain lengths added, and (b) Tafel slope plots. (The negative sign indicates the direction of current, not its magnitude.)

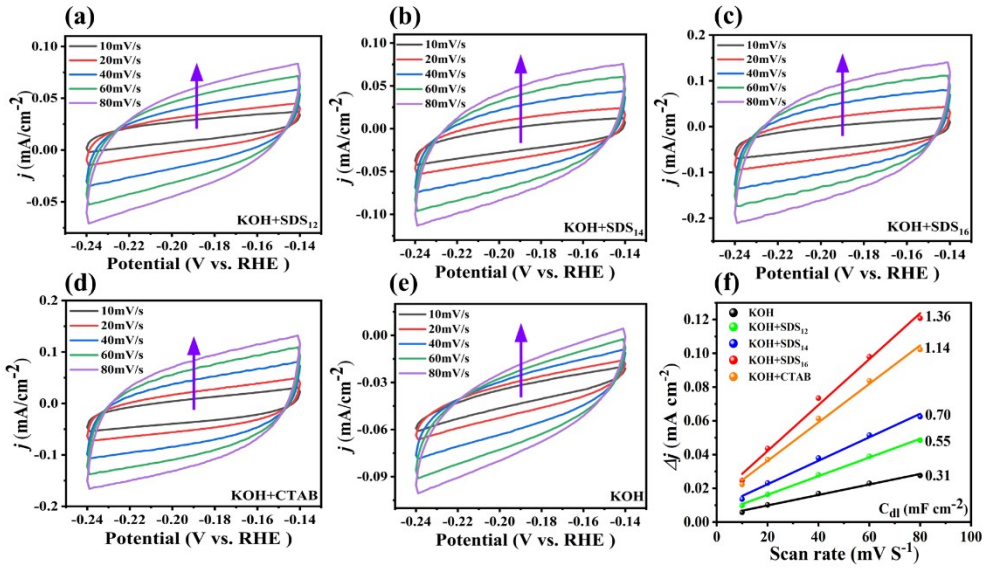

Fig. S15 CV profiles of the Cu-catalyst at various scan rates were systematically studied in 1 M KOH electrolytes with and without cationic/anionic surfactants. The electrolyte compositions are: (a) 1 M KOH + 0.05 mM SDS_{12}, (b) 1 M KOH + 0.05 mM SDS_{14}, (c) 1 M KOH + 0.05 mM SDS_{16}, (d) 1 M KOH + 0.05 mM CTAB, and (e) pure 1 M KOH. (f) The double-layer capacitance (C_{dl}) was determined from the linear regression of the charging current density difference (Δj) between the anodic and cathodic scans versus the scan rate.

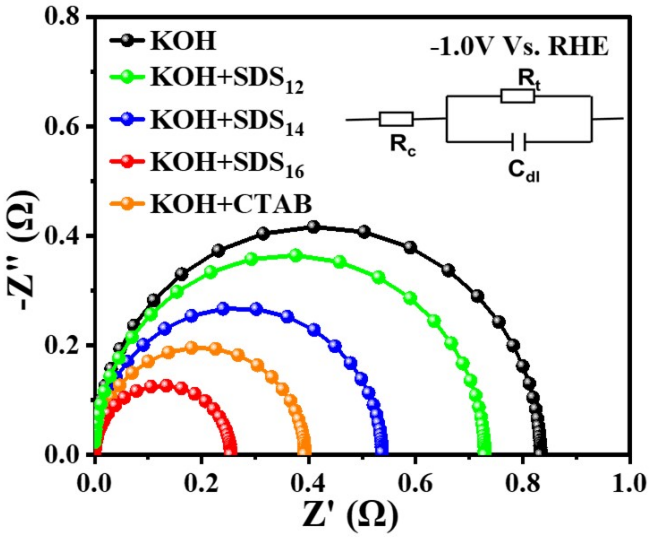

Fig. S16 EIS measurement datas under different electrolyte conditions.

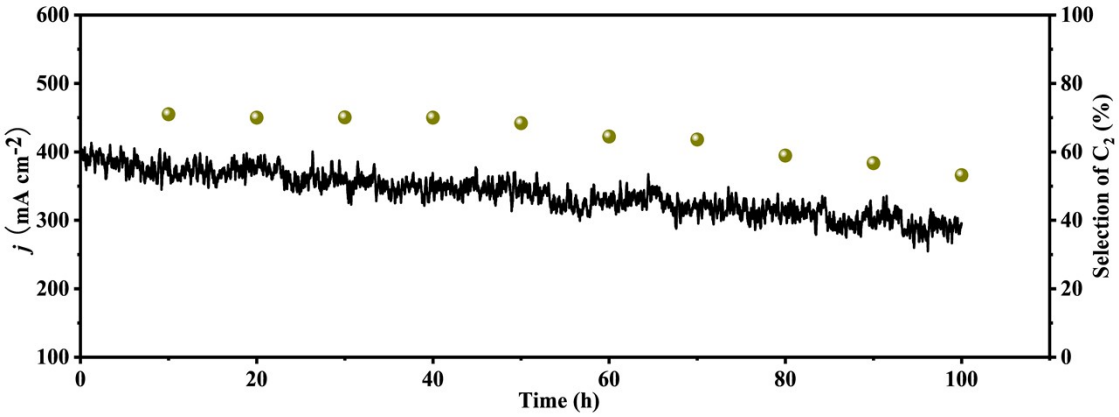

Fig. S17 The timing current stability of anionic surfactant SDS_{16} modified 1 M KOH electrolyte under -1.0 V vs. RHE conditions.

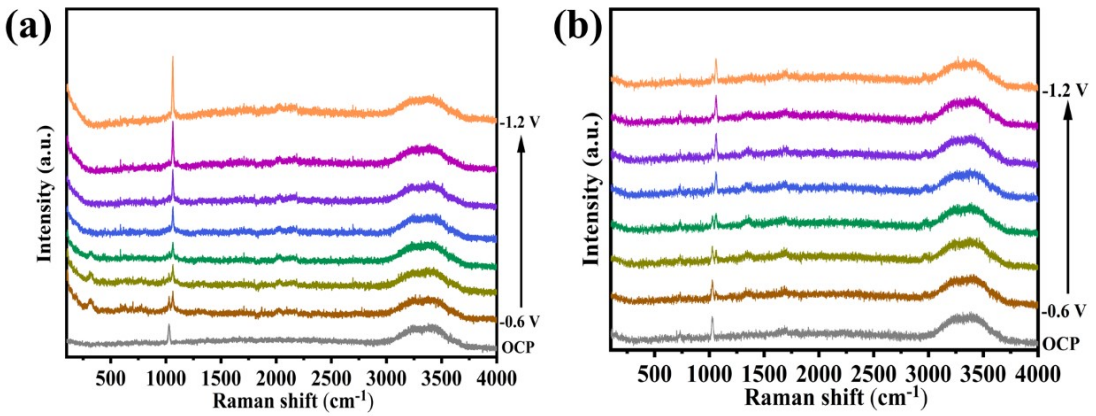

Fig. S18 In-situ Raman spectroscopy analysis of the catalyst. In-situ Raman spectroscopy-Full spectrum (a) Cu_x(KOH+SDS_{16}), and(b) Cu_x(KOH+CTAB)at different potentials.

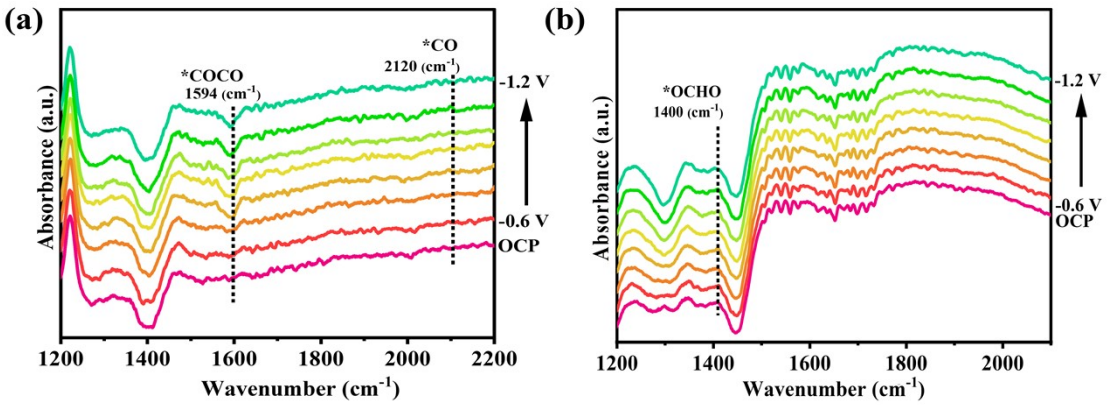

Fig. S19 In ATR-SEIRAS analysis of the catalysts. (a) Cu_x(KOH+SDS_{16}), and(b) Cu_x(KOH+CTAB)at different potentials.

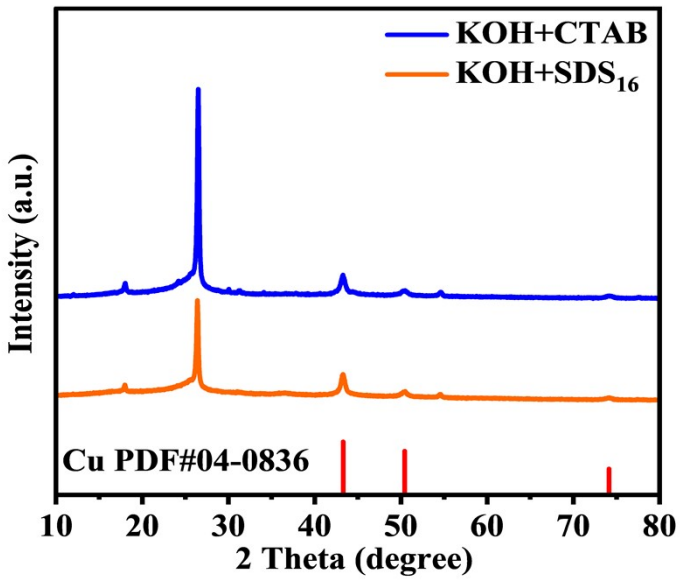

Fig. S20 After the 100 h stability test, the XRD spectrum of the catalysts.

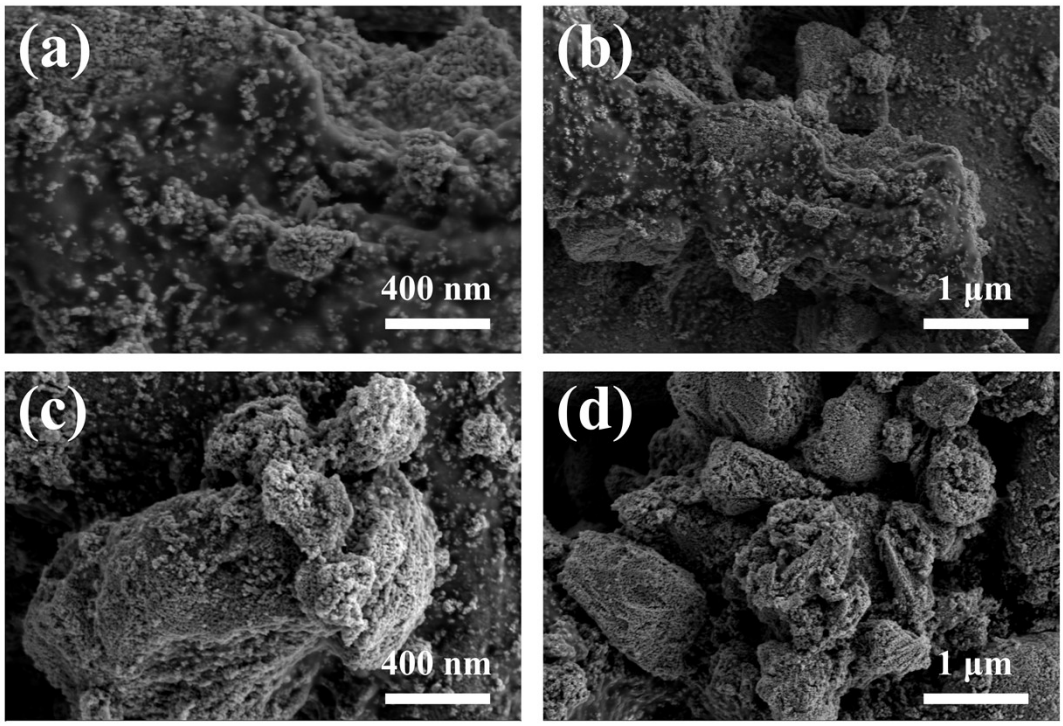

Fig. S21 After the 100 h stability test, the SEM spectrum of the catalyst. (a-b) Cu_x(KOH+ SDS_{16}), (c-b) Cu_x(KOH+CTAB).

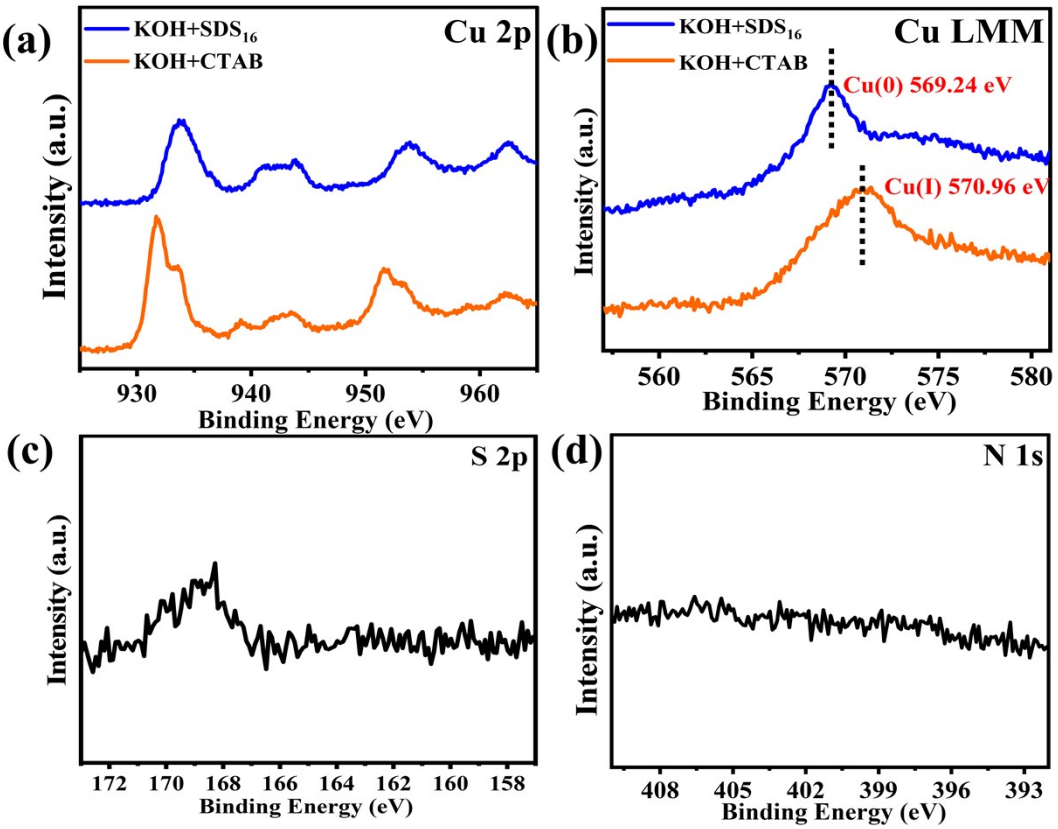

Fig. S22 After the 100 h stability test, the XPS spectrum of the catalysts.(a) Cu 2p, (b) Cu LMM, (c) S 2p, (d) N 1s.

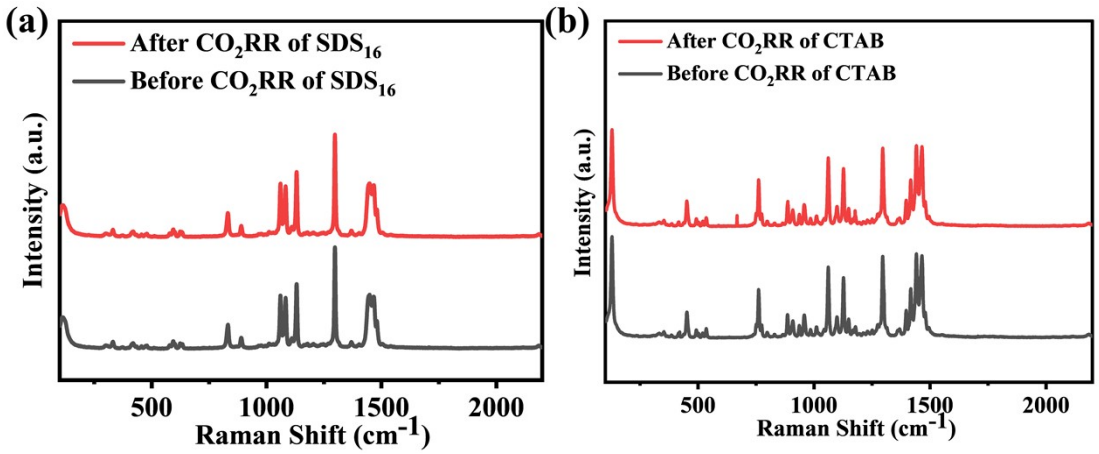

Fig. S23 The Raman spectra of the surfactant in the electrolyte before and after the 100 h stability test. (a) SDS_{16}, (b) CTAB.

Table. S1 CO_2RR performance of copper-based catalysts: surfactant modification vs. traditional optimization strategies.[4–8]

Catalyst	Surfactant	Electrolyte	Product	FE (%)	J (mA cm^{-2})	Potentiual (V vs. RHE)	Stability (h)	Ref.
This work: Cu_x(KOH+SDS_{16}/CTAB)	SDS_{16}/CTAB	1 M KOH	C_2/HCOOH	70.1 /71.31	-390	-1.0	100	This work
1-M Cu	Gemini surfactants	1 M KOH	HCOOH	96	N/A	-0.7	20	[4]
Cu_2O@Cu	CTAB	0.5 M $KHCO_3$	$HCOO^-$	> 90	-146.4	-0.9	24	[5]
Cu foil	CTAB	0.1 M $NaHCO_3$	HCOOH	50	N/A	-0.6	8	[6]
Cu@SDS	SDS	1 M KOH	C_2	86	-231	-0.8	18	[7]
OD-Cu	TBAN	1 M KOH	C_{2+}	78	-765	-0.65	10	[8]

Table. S2 CO_2RR performance of copper-based catalysts: surfactant modification vs. traditional optimization strategies.[9–13]

Strategy	Catalyst	Electrolyte	Potential (V vs. RHE)	Product	FE (%)	Current Density (mA cm^{-2})	Stability (h)	Year	Ref.
Surfactant Modification	Cu_x(KOH+SDS_{16}/CTAB)	1 M KOH	-1.0	C_2/HCOOH	70.1	-390	100	2025	This work
Crystal surface control	Ag/h-Cu_2O(100)	0.1 M $KHCO_3$	-0.96	CO	93	-6.5	20	2024	[9]
Crystal surface control	SCF3 Cu(111)/(200)	1 M KOH	-1.6	C_2	70.6	149.5	8	2025	[10]
Crystal surface control	p-Cu(100)	1 M KCl	-1.4	C_2H_4	72	500	>100	2024	[11]
Alloying	Pd_4Ag_1 NSs	0.1 M $KHCO_3$	-0.1	$HCOO^-$	99.4	-400	4.17	2025	[12]
Alloying	CuO-SnO_2 NFs	1 M KOH	-0.99	HCOOH	65.3	-300	6	2024	[13]

References

1 D. A. Svintsitskiy, T. Yu. Kardash, O. A. Stonkus, E. M. Slavinskaya, A. I. Stadnichenko, S. V. Koscheev, A. P. Chupakhin and A. I. Boronin, *J. Phys. Chem. C*, 2013, **117**, 14588–14599.

2 L. Zhou, C. Li, J. J. Lv, W. Wang, S. Zhu, J. Li, Y. Yuan, Z. J. Wang, Q. Zhang, H. Jin and S. Wang, *Carbon Energy*, 2023, **5**, e328.

3 Y. Song, C. B. Musgrave, J. Su, L. Huang, W. Guo, Y. Liu, G. Li, Y. Xin, Q. Zhang, X. Feng, C. Liao, S. Liu, R. T. K. Kwok, J. W. Y. Lam, M. He, K. S. Choong, Z. Feng, B. Z. Tang, W. A. Goddard and R. Ye, *Nat. Nanotechnol.*, 2026, **21**, 78–86.

4 X. Zhang, X. Yan, P. Chen, P. Zhang, X. Kang, J. Ma, C. Chen and B. Han, *Angew. Chem. Int. Ed.*, 2024, **63**, e202315822.

5 S. Qiao, G. Zhang, D. Tian, W. Xu, W. Jiang, Y. Cao, J. Qian, J. Zhang, Q. He and L. Song, *Energy Environ. Sci.*, 2024, **17**, 6779–6786.

6 S. Banerjee, X. Han and V. S. Thoi, *ACS Catal.*, 2019, **9**, 5631–5637.

7 Y. Wang, R. Zhao, Y. Liu, F. Zhang, Y. Wang, Z. Wu, B. Han and Z. Liu, *Chem. Sci.*, 2024, **15**, 4141–4145.

8 M. P. L. Kang, H. Ma, R. Ganganahalli and B. S. Yeo, *ACS Catal.*, 2024, **14**, 116–123.

9 J. Li, Z. Cheng, J. Zhu, H. Chen, X. Xu, Y. Wang, J. Liu, Z. Xu and L. Wang, *Appl. Catal. B Environ. Energy*, 2024, **352**, 124049.

10 Y. C. Zhang, X. L. Zhang, Z. Z. Wu, Z. Z. Niu, L. P. Chi, F. Y. Gao, P. P. Yang, Y. H. Wang, P. C. Yu, J. W. Duanmu, S.-P. Sun and M. R. Gao, *Proc. Natl. Acad. Sci.*, 2024, **121**, e2400546121.

11 R. Niu, H. Xiao, B. Xu, G. Li, D. Tan, B. Lin and G. Yang, *J. Catal.*, 2025, **452**, 116408.

12 S. Sun, M. Liu, Y. Mao, F. Liu, X. Xu, Y. Li, X. Lv, S. Zhao, X. Liu, Y. Wu and Y. Chen, *Dalton Trans.*, 2025, **54**, 8306–8316.

13 S. Go, W. Kwon, D. Hong, T. Lee, S. H. Oh, D. Bae, J. H. Kim, S. Lim, Y. C. Joo and D. H. Nam, *Nanoscale Horiz.*, 2024, **9**, 2295–2305.